



1 **Fractional solubility of iron in mineral dust aerosols over coastal**
2 **Namibia: a link with marine biogenic emissions?**

3

4 **Karine Desboeufs¹, Paola Formenti¹, Raquel Torres-Sánchez^{2,3}, Kerstin Schepanski^{4,§}, Jean-**
5 **Pierre Chaboureau⁵, Hendrik Andersen^{6,7}, Jan Cermak^{6,7}, Stefanie Feuerstein⁴, Benoit Laurent¹,**
6 **Danitza Klopper^{8,*}, Andreas Namwoonde⁹, Mathieu Cazaunau², Servanne Chevaillier², Anaïs**
7 **Feron^{1,%}, Cécile Mirande-Bret¹, Sylvain Triquet¹, and Stuart J. Piketh⁸**

8

9

10 ¹ Université Paris Cité and Université Paris Est Créteil, CNRS, LISA, F-75013 Paris, France

11 ² Université Paris Est Créteil and Université Paris Cité, CNRS, LISA, F-94010 Créteil, France

12 ³ CIQSO, Robert H. Grubbs Building, University of Huelva, Campus El Carmen, E21071 Huelva, Spain

13 ⁴ TROPOS, Leipzig, Germany

14 ⁵ Laboratoire d'Aérodynamique (LAERO), Université de Toulouse, CNRS, UT3, IRD Toulouse, France

15 ⁶ Institute of Meteorology and Climate Research, Karlsruhe Institute of Technology (KIT), Karlsruhe,
16 Germany

17 ⁷ Institute of Photogrammetry and Remote Sensing, Karlsruhe Institute of Technology (KIT), Karls-
18 ruhe, Germany

19 ⁸ North-West University, School for Geo- and Spatial Sciences, Potchefstroom, South Africa

20 ⁹ SANUMARC, University of Namibia, Henties Bay, Namibia

21

22 * Now at University of Limpopo, Department of Geography and Environmental Studies, Sovenga,
23 South Africa

24 [§] Now Institute of Meteorology, Freie Universität Berlin, Berlin, Germany

25 [%] Now at Université Paris-Saclay, INRAE, AgroParisTech, UMR ECOSYS, Palaiseau, France

26

27 **Corresponding author:** paola.formenti@lisa.ipsl.fr

28



29 **Abstract**

30 Mineral dust is the largest contributor to elemental iron in the atmosphere, and, by deposition, to the
31 oceans, where elemental iron is the main limiting nutrient. Southern Africa is an important source at
32 the regional scale, and for the Southern Ocean, however limited knowledge is currently available
33 about the fractional solubility of iron from those sources, as well as on the atmospheric processes
34 conditioning its dissolution during deposition.

35 This paper presents the first investigation of the solubility of iron in mineral dust aerosols from 176
36 filter samples collected at the Henties Bay Aerosol Observatory (HBAO), in Namibia, from April to
37 December 2017. During the study period, 10 intense dust events occurred. Elemental iron reached
38 peak concentrations as high as $1.5 \mu\text{g m}^{-3}$, significantly higher than background levels. These events
39 are attributed to wind erosion of natural soils from the surrounding gravel plains of the Namib desert.
40 The composition of the sampled dust is found to be overall similar to that of aerosols from northern
41 Africa, but characterised by persistent and high concentrations of fluorine, which are attributed to
42 fugitive dust from mining activities and soil labouring for construction.

43 The fractional solubility of Fe (%SFe) for both the identified dust episodes and background conditions
44 ranged between 1.3 to 20 %, in the range of values previously observed in the remote Southern
45 Ocean. Even in background conditions, the iron fractional solubility was correlated to aluminium and
46 silicon solubility. The solubility was lower between June and August, and increased from September
47 onwards, during the austral spring months. The relation with measured concentrations of particulate
48 MSA (methanesulfonic acid), solar irradiance and wind speed suggests a possible two-way interaction
49 whereby marine biogenic emissions from the coastal Benguela upwelling to the atmosphere would
50 increase the solubility of iron-bearing dust, according to the photo-reduction processes proposed by
51 Johansen and Key (2006). The subsequent deposition of soluble iron could act to further enhance
52 marine biogenic emissions. This first investigation points to the west coast of southern Africa as a
53 complex and dynamic environment with multiple processes and active exchanges between the at-
54 mosphere and the Atlantic Ocean, requiring further research.

55

56 **Keywords:** aerosols, mineral dust, water-soluble Fe, atmospheric processing, marine biogenic emis-
57 sions



58 **1. Introduction**

59 Through the processes of atmospheric transport and deposition, mineral dust is known to provide
60 nutrients and metals to the terrestrial and marine ecosystems (Hooper et al., 2019; Ventura et al.,
61 2021). Amongst those, mineral dust provides iron (Jickells et al., 2005), which plays a major role for
62 the primary productivity of the nutrient-limited oceans, modulating the marine carbon cycle (Hooper
63 et al., 2019) as well as that of key continental ecosystems such as the Amazon rainforest (Reichholf,
64 1986).

65 To date, much attention has been paid to the soluble Fe in mineral dust emitted from arid and semi-
66 arid areas in the northern Hemisphere, in particular the Saharan and Chinese deserts (e.g. Baker et
67 al., 2006; Paris et al., 2010; Takahashi et al., 2011; Rodriguez et al., 2021), where emissions are the
68 most intense (Tegen and Schepanski, 2009).

69 Nonetheless, the southern Hemisphere accounts for approximately 10% of the global atmospheric
70 dust loading (Kok et al., 2017). Large sources are found in southern Africa, mostly in Namibia (Kala-
71 hari and Namib deserts, Etosha Pan), numerous ephemeral riverbeds along the Namibian coastline
72 and Botswana (Makgadikgadi Pan; Prospero et al., 2002; Bryant et al., 2007; Mahowald et al., 2003;
73 Ginoux et al., 2012; Vickery and Eckardt, 2013; Von Holdt et al., 2017).

74 Previous research has shown that the long-range transport of dust emitted from southern African
75 sources can reach the south-eastern Atlantic and the Indian Oceans (Swap et al., 1996; Jickells et
76 al., 2005; Bhattachan et al., 2012; 2015; Ito and Kok, 2017). In particular, Gili et al. (2022) demon-
77 strated recently that mineral dust from Namibia can be transported across the Southern Ocean to
78 eastern Antarctica. Furthermore, the research by Dansie et al. (2022) has suggested that mineral dust
79 from Namibia could dominate the atmospheric deposition to the coastal Benguela Upwelling System
80 (BUS), where biomass burning aerosols, a significant source of soluble Fe to the Southern and Indian
81 Oceans (Hamilton et al., 2021; Ito et al., 2021; Liu, et al., 2022), are limited by atmospheric stratifica-
82 tion (Formenti et al., 2019; Redemann et al., 2021).

83 There is, however, very little data available on the concentrations and composition of soluble Fe in
84 dust aerosols from southern Africa, both near the sources and over the oceans. Previous research in
85 Namibia focussed on soils and sediments (Dansie et al., 2017a; 2017b; Kanguuehi, 2021). The At-
86 lantic Meridional Transect (AMT) cruise programme conducted recurrent observations between Oc-
87 tober and March in the South Atlantic Ocean (Baker et al., 2013), while Heimbürger et al. (2013) and
88 Gao et al. (2013) report on sparse measurements of deposited aerosols and in rainwaters over the
89 Southern Indian Ocean.

90 Within this context, this paper investigates the fractional solubility of Fe in samples of atmospheric
91 aerosol particles smaller than 10 μm in diameter collected in 2017 at the Henties Bay Aerosols Ob-
92 servatory (HBAO; 22.09°S, 14.26°E) on the Namibian coast. In section 2 we outline the experimental



93 and analytical methodology for elemental and water-soluble analysis of ions and metals, including
94 iron, obtained by Inductively Coupled Plasma (ICP) analysis. We also provide the definition of frac-
95 tional solubility and method for estimating the total dust mass. We introduce the supporting tools used
96 to evaluate the source regions of the collected mineral dust, their pathways during transport, and the
97 presence of fog, a recurrent feature on coastal Namibia favouring multi-phase ageing processes.
98 Section 3 provides the results of the analysis. We present the iron soluble concentrations and solu-
99 bility, and explore their links to the load, emission area and transport of mineral dust, as well as at-
100 mospheric processing. Section 4 discusses the observations, suggesting that the fractional solubility
101 of iron in the Namibian dust is higher when the particulate MSA, a tracer of marine biogenic emissions,
102 is also detected in highest concentrations. This points to the photo-oxidation of DMS as a process for
103 increasing the dust solubility, and suggests a possible positive feedback loop of the iron fertilisation
104 by dust to the ocean. Section 5 summarizes the findings and suggests directions for future research.

105

106 2. Methodology

107 2.1. Study area

108 The Henties Bay Aerosol Observatory (HBAO, 22.09°S, 14.26°E; <http://www.hbao.cnrs.fr/>, last ac-
109 cess: 10 October 2022) is located at the Sam Nujoma Marine and Coastal Resources Research Cen-
110 tre (SANUMARC) of the University of Namibia in Henties Bay, Namibia (**Fig 1**).



111

112 **Fig 1.** Location of Henties Bay Aerosol Observatory (HBAO, red star) and main dust source regions (©
113 Google Maps). The position of Walvis Bay (blue dot), the major harbour in the area, and the Wlotzkasbaken
114 meteorological station (blue star) are also indicated.



115

116 Three kilometers to the south of the University campus hosting HBAO is the small town of Henties
117 Bay, with no industrial activity and very little traffic, and approximately 170 km north from Walvis Bay,
118 the major harbour in Namibia. Directly east of HBAO are the Namibian gravel plains, which are one
119 of the dominant features of the Namib desert together with the sand dunes. Approximately 100 m to
120 the north is the Omaruru riverbed, one of the coastal sources of mineral dust identified by Vickery and
121 Eckardt (2013).

122 Our previous results show that, at the surface level, the atmosphere at HBAO is a receptor of different
123 air masses dominated by marine aerosols, but also the seasonal occurrence of light-absorbing aero-
124 sols from biomass burning or pollution in northern wind regimes, and mineral dust detected episodically
125 from various wind directions (Formenti et al., 2018; Klopper et al., 2020, hereafter KL20).

126 **2.2. Sample collection and analysis**

127 Aerosol particles smaller than 10 μm in aerodynamic diameter (PM_{10}) were collected by an automated
128 sampler (model Partisol Plus 2025i, Thermo Fisher Scientific, Waltham, MA USA) on 47 mm What-
129 man Nuclepore polycarbonate filters (1- μm pore size). The air was drawn through a certified sampling
130 inlet (Rupprecht and Patashnick, Albany, New York, USA) located at approximately 30 m above
131 ground and operated at a flow rate of 1 $\text{m}^3 \text{h}^{-1}$. Samples were collected for 9 hours during the daytime
132 (from 9:00 to 18:00 UTC time) and night-time (21:00 to 06:00 UTC time) for 12 non-consecutive weeks
133 from April to December 2017 (7-14 April, 26 April-3 May, 19-26 May, 07-14 July, 2-9 August, 15-22
134 August, 18-25 September, 02-09 October, 31 October-7 November, 13-20 November, 28 November-
135 04 December, 12-19 December). In total, 176 samples (including 13 blanks, one per week of sam-
136 pling) were collected.

137 The elemental analysis of 24 elements from Na to Pb and including some major tracers of mineral
138 dust (Fe, Al and Si) was performed at the LISA laboratory by Wavelength-dispersive X-ray fluores-
139 cence (WD-XRF) using a PW-2404 spectrometer (Panalytical, Almelo, Netherlands), as detailed by
140 KL20. The total mass concentration per element x will be referred to as T_x .

141 The measured elemental concentrations are used to calculate the estimated dust mass (*EDM*) ac-
142 cording to Lide (1992) as

$$143 \text{ EDM} = 1.12 \times \{1.658 \times [\text{nss-Mg}] + 1.889 \times [\text{Al}] + 2.139 \times [\text{Si}] + 1.399 \times [\text{nss-Ca}] + 1.668 \times [\text{Ti}] + 1.582$$
$$144 \quad \times [\text{Mn}] + (0.5 \times 1.286 + 0.5 \times 1.429 + 0.47 \times 1.204) \times [\text{Fe}]\} \quad (1)$$

145

146 where, as explained by KL20, nss-Mg and nss-Ca represent the non-sea salt fractions of Mg and Ca,
147 respectively.



148 The analysis of the water-soluble fraction was also performed at LISA. Individual filters were placed
149 in 20 mL of ultrapure water (MilliQ® 18.2 MΩ.cm) for 30 minutes. The solution was then divided into
150 two sub-samples. One half was analysed by Ion chromatography (IC) using a Metrohm IC 850 device
151 equipped with a column MetrosepA supp 7 (250/4.0 mm) for anions and with a Metrosep C4 (250/4.0
152 mm) for cations. The IC analysis provided the concentrations of the following water-soluble ions: for-
153 mate, acetate, MSA⁻ (methanesulfonic acid), Cl⁻, NO₃⁻, SO₄²⁻, oxalate, Na⁺, NH₄⁺, K⁺, Ca²⁺ and Mg²⁺.
154 A calibration with certified standard multi-ions solutions of concentrations ranging from 5 to 5000 ppb
155 was performed and the uncertainty of the analysis was estimated to be 5% (KL20).

156 The second half of the solution was acidified to 1% with ultrapure nitric acid (HNO₃) and analysed by
157 Inductively Coupled Plasma-Atomic Emission Spectroscopy (ICP-AES) using a Spectro ARCOS
158 Ametek® ICP-AES and by High-resolution Inductively Coupled Plasma-Mass Spectrometry (HR-ICP-
159 MS) using a Neptune Plus™ instrument by Thermo Scientific™. The calibration curve was performed
160 using standard multi-element solutions ranging from 2 to 1000 ppb for ICP-AES and 1 to 1000 ppt for
161 HR-ICP-MS (Desboeufs et al., 2022). These analyses provided the dissolved mass concentrations
162 (D_x) of 25 water-soluble metals and metalloids, including Fe, Al, and Si. All sample concentrations
163 were corrected using the filter blanks for each sampling period.

164 Based on those analyses, the fractional solubility (%S_x) representing the percentage solubility value
165 was calculated as

166

$$167 \quad \%S_x = 100 \times D_x/T_x \quad (2)$$

168

169 with D_x and T_x, the dissolved and total elemental concentration respectively.

170 **2.3. Ancillary data**

171 Maps of the emission fluxes of mineral dust were calculated using the dust emission model described
172 by Feuerstein and Schepanski (2019), driven with hourly 10m wind fields at a 0.1° x 0.1° grid from
173 the European Centre for Medium-range Weather Forecasts (ECMWF). The dust emission parame-
174 terisation follows Marticorena and Bergametti (1995). Additional information on the soil type was taken
175 from the ISRC soil data set (FAO/IIASA/ISRIC/ISSCAS/JRC, 2012) and information on the aerody-
176 namic roughness length was obtained from POLDER/ADEOS surface products following the works
177 of Marticorena et al. (2004) and Laurent et al. (2005). The MODIS monthly vegetation product
178 (MYD13A3 v6) was used to describe the vegetation cover, while the vegetation type was defined
179 using the BIOME4 database (Kaplan et al., 2003). We additionally differentiated between different
180 dust source types (alluvial fines, dunes and sand sheets) which allowed us to reflect the source di-
181 versity over Namibia and thus the spatial diversity in the soil's susceptibility to wind erosion. This layer



182 was compiled following Feuerstein and Schepanski (2019) using MODIS surface reflectance
183 (MOD09A1 v6). A MODIS retrieved map on surface water cover was used to eliminate flooded areas
184 as active dust sources.

185 Back-trajectories of the air masses during the dust event were calculated from Meso-NH model (ver-
186 sion 5.3). The model set-up is similar to the one used for the AErosols, RadiatiOn and CLOUDs in
187 southern Africa (AEROCLO-sA) field campaign (Formenti et al. 2019) and related case studies (Fla-
188 mant et al. 2022; Chaboureau et al. 2022). In short, the model was run on a 5 km grid covering the
189 southern tip of Africa and 67 stretched levels spaced by 60 m close to the surface and 600 m at high
190 altitude. Meso-NH was run for 24 h for each dust event using initial and boundary conditions provided
191 by the ECMWF operational analysis. Emission, transport and deposition of dust is described by the
192 scheme of Grini et al. (2006). Back trajectories were computed online using three passive tracers
193 initialized with the 3D-field of their initial conditions. Further details on the dust prognostic scheme,
194 the backward trajectories and the physical parameterizations are given in Chaboureau et al. (2022).

195 The presence of fog and low clouds (FLC) along the Namibian coastline during dust events was an-
196 alysed using an existing satellite-based fog and low-cloud data set (Andersen et al., 2019). The FLC
197 detection algorithm used to create this data set was developed and validated specifically for this re-
198 gion. The algorithm is based on infrared observations from the Spinning Enhanced Visible and Infra-
199 red Imager (SEVIRI) aboard the geostationary Meteosat Second Generation (MSG) satellites, making
200 use of both spectral and textural information. The FLC product is available at the native spatial and
201 temporal resolutions of the SEVIRI sensor (3 km nadir, every 15 minutes), as described in Andersen
202 and Cermak (2018). The FLC product does not specifically distinguish between fog and low clouds
203 but captures the coastal boundary-layer cloud regime typical for the region and at HBAO that could
204 interact with mineral dust. It has been shown to be consistent with synoptic-scale atmospheric dy-
205 namics (Andersen et al. 2020). The FLC data are used to calculate maps of average fog and low
206 cloud coverage for the time periods of all dust events given in Table 1.

207 Observations of the local meteorology, including measurements of air temperature, relative humidity
208 and fog, at the nearby Wlotzkasbaken meteorological station (22.31°S, 14.45°E, 73 m asl, see **Fig.**
209 **1**) part of the Southern African Science Service Centre for Climate Change and Adaptive Land Man-
210 agement (SASSCAL) ObservationNet (<https://www.sasscal.org/>; last accessed 14/04/2023), are
211 used.

212

213 **3. Results**

214 **3.1. Description of the dust episodes**



215 The dataset discussed in this paper is based on 176 aerosol samples collected at HBAO, 42 of which
 216 were associated with 10 dust episodes. As detailed by KL20, events of mineral dust were identified
 217 as peaks in the time series of the mass concentrations of Al and non-sea-salt Ca²⁺ (nss-Ca²⁺). The
 218 dust episodes investigated in this study are a subset of those presented by KL20, we therefore use
 219 their naming convention to facilitate the connections between the two papers (**Table 1**). In the follow-
 220 ing, we refer to samples collected during the dust episodes as “dust”. Samples collected outside the
 221 dust events will be indicated as “background”.

222
 223 **Table 1.** Dates of dust events identified at HBAO from May to December 2017, following KL20. The number of
 224 samples collected during each episode is indicated in the column called “N”. The average air temperature,
 225 relative humidity, wind speed and direction recorded at the nearby meteorological station in Wlotzkasbaken are
 226 reported. The maxima wind speed and corresponding direction are indicated in brackets in the corresponding
 227 columns. The average EDM is reported with in brackets the maximum of EDM during the event.

Episode identifier	Start and end date (UTC)	N	Air temperature (°C)	RH (%)	Wind speed (m s ⁻¹)	Wind direction (degN)	EDM (µg m ⁻³)
Dust 04	19/05 09h – 20/05 18h	3	17.7	73.7	2.7 (6.2)	186 (185)	13 (14)
Dust 05	24/05 21h – 26/05 09h	3	18.1	63.3	2.3 (6.3)	183 (188)	21 (42)
Dust 06	11/07 09h – 13/07 09h	4	13.2	82.9	1.2 (5.4)	235 (193)	27 (45)
Dust 07	04/08 21h – 06/08 09h	4	12.5	87.0	1.2 (5.4)	233 (201)	10 (16)
Dust 08	17/08 21h – 19/08 09 h	4	11.9	80.6	1.3 (4.6)	324(129)	18 (21)
Dust 09	23/09 21h – 24/09 18h	2	15.6	84.3	3.1 (6.2)	309 (330)	11 (17)
Dust 10	05/10 21h – 08/10 09h	8	14.0	74.6	2.1 (5.9)	249 (228)	14 (23)
Dust 11	15/11 09h – 18/11 09h	6	16.7	66.1	3.2 (11.7)	231 (232)	31 (56)
Dust 12	30/11 09h – 01/12 18h	3	16.7	78.1	1.9 (5.7)	244 (195)	2 (3)
Dust 13	15/12 09h – 19/12 09h	7	16.9	76.9	2.9 (6.5)	252 (238)	10 (19)

228

229 The dust episodes were long-lasting (generally a few days). The dynamic of the emissive areas, air
 230 mass transport and fog coverage during the episodes (**Fig. S1**) is driven by the synoptic circulation,
 231 which, in southern Africa, is primarily affected by the high-pressure belt under the descending limb of
 232 the Hadley cell (Tyson and Preston-Whyte, 2014). The maps of dust emission fluxes and the air mass
 233 back-trajectories reflect this seasonality. During the first part of the year (episodes Dust 04 to 05),
 234 dust emissions originated from the gravel plains and the Etosha pan north of HBAO. During this time
 235 of the year the transport to HBAO below 300 m asl was north- to south-easterly originating inland from
 236 the coast.

237 From July onwards, the active source areas were identified in the southern gravel plains, Namib sand
 238 dunes and Kalahari Desert (this former only for Dust 11 to 13). Air mass transport was southerly and
 239 travelled over the sea and along the coastline. It is worth noticing that all the air masses experienced



240 maritime air during their last hours of transport, including the episodes Dust 04 and 05 associated
 241 with berg wind conditions, due to the coastal low that develops to the west of HBAO.

242 The formation of fog events at Henties Bay is also highly seasonal. The frequency of occurrence of
 243 fog events is highest during austral winter at the coast, whereas lifted stratus clouds dominate during
 244 austral summer, when overall FLC occurrence peaks. The occurrence of fog over Namibia correspond
 245 to the advection of low-level clouds which is modulated both by local meteorology along the coastline
 246 of Namibia and synoptic-scale radiative processes (Spirig et al., 2019; Andersen et al., 2019; 2020).
 247 Henceforth, as shown in Fig. S1, the presence of fog and low clouds correlates with wind directions
 248 and aerosol source regions. Overall, three episodes (Dust 04, Dust 05 and Dust 11 in April, May and
 249 November, respectively) occurred in fog-free or low-fog conditions. The remaining episodes were
 250 characterised by extensive fog and low cloud coverage throughout the study area. The meteorological
 251 observations at the nearby Wlotzkasbaken station (**Fig. S2**) confirm these findings, and show in par-
 252 ticular that the relative humidity always exceeded 60 %, and 80 % when fog or low clouds were pre-
 253 sent (Table 1). As a consequence, the aerosol can be considered deliquescent even in the fog-free
 254 conditions. The seasonality is also observed in the average downwelling solar irradiance, with the
 255 lowest values during July and September, associated with austral winter. Finally, it is interesting to
 256 note that the fog-free conditions, associated with the predominance of continental air masses, corre-
 257 sponded to the highest estimated dust mass (EDM), possibly because of the reduced wet removal
 258 during transport and the increase of emission fluxes with the decrease of soil moisture (Kok et al.,
 259 2014), but possibly also because of the high wind speed prevailing during these conditions, which in
 260 principle, enhancing both dust emissions and transport (Table 1).

261 3.2. Iron solubility

262 The total and dissolved concentrations, and fractional solubility of Fe, Al and Si, during the dust epi-
 263 sodes are reported in **Table 2**, where they are compared to background conditions. For iron, the
 264 average values over the entire sampling period are also shown.

265 **Table 2.** Average and standard deviations of water-soluble (Dx), total elemental (Tx) mass concentrations and
 266 fractional solubility (%Sx) for Fe, Al and Si at HBAO measured for the total period and during the dust and
 267 background events from April to December 2017. Concentrations values are expressed in ng m^{-3} , while frac-
 268 tional solubility is expressed in percent. The numbers of considered samples is presented between the paren-
 269 theses.

	Fe			Al		Si	
	All period	Dust	Background	Dust	Background	Dust	Background
Dx	28 ± 51 (N=175)	80 ± 84 (N=42)	11 ± 10 (N=131)	322 ± 296 (N=42)	56 ± 46 (N=131)	529 ± 616 (N=42)	78 ± 83 (N=124)
Tx	364 ± 482 (N=176)	955 ± 633 (N=42)	177 ± 155 (N=133)	1204 ± 870 (N=42)	284 ± 222 (N=94)	4158 ± 3037 (N=42)	776 ± 674 (N=133)
%Sx	7.1 ± 3.6 (N=175)	7.9 ± 4.1 (N=42)	6.8 ± 3.3 (N=130)	27 ± 10 (N=42)	26 ± 11 (N=90)	12 ± 7 (N=42)	11 ± 8 (N=116)



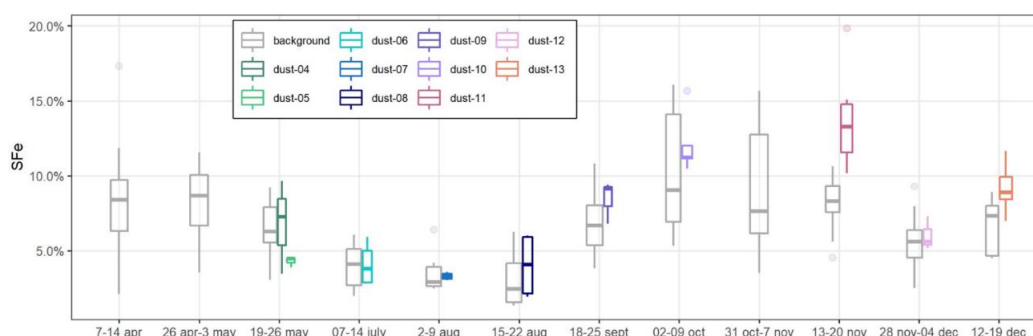
270

271 The total Fe concentrations varied significantly from one episode to the other, and so did EDM, which
 272 was larger than $10 \mu\text{g m}^{-3}$ for all of them (except Dust 12) and as high as $56 \mu\text{g m}^{-3}$ during Dust 11
 273 event (Table 1). By contrast, the total Fe-to-EDM ratio was virtually constant, with an average of 5.8
 274 % (± 0.6 %) for the dust events and 5.6 % (± 1.1 %) for the entire dataset.

275 The total dissolved concentrations of Fe during the sampling period ranged from 1.5 to 427 ng m^{-3} ,
 276 with a median and average of 10.5 and 28 ng m^{-3} . During the dust episodes, the average mass con-
 277 centration of dissolved Fe was $80 \pm 84 \text{ ng m}^{-3}$, almost an order of magnitude higher than for back-
 278 ground conditions ($11 \pm 10 \text{ ng m}^{-3}$). The dissolved concentrations in dust periods are higher than
 279 those observed in the South Atlantic Ocean for air masses associated with transport from continental
 280 southern Africa (Baker et al., 2013; Chance et al., 2015; Baker and Jickells, 2017), which are of the
 281 order as those observed at HBAO for background periods.

282 The calculated fractional solubility of Fe ranged from 1.3 to 19.8 %, with a median and average of 6.7
 283 and 7.1 %. The average %SFe during dust events (7.9 ± 4.1 %) was higher than in background con-
 284 ditions (6.8 ± 3.3 %). It is interesting to note that Dust 11 event, the most intense recorded event,
 285 presents the highest %SFe (between 10.2 and 19.8 % with an average at 13.8 %). Apart from this
 286 event, the average fractional solubility seems to be independent of the EDM. Excluding this event, the
 287 average solubility of Fe for dust event (6.9 ± 3.3 %) is equivalent to the one for background samples.
 288 For both conditions, the observed range of variability is high and consistent with previous observations
 289 (2.4-20 %, Baker et al., 2013; 1.3-22 %, Chance et al., 2015), as well as with measurements over the
 290 Southern Indian Ocean (0.76-27 %, Gao et al., 2013).

291 The temporal variability of %SFe is presented in **Fig. 2**, where dust and background episodes are
 292 shown separately.



293

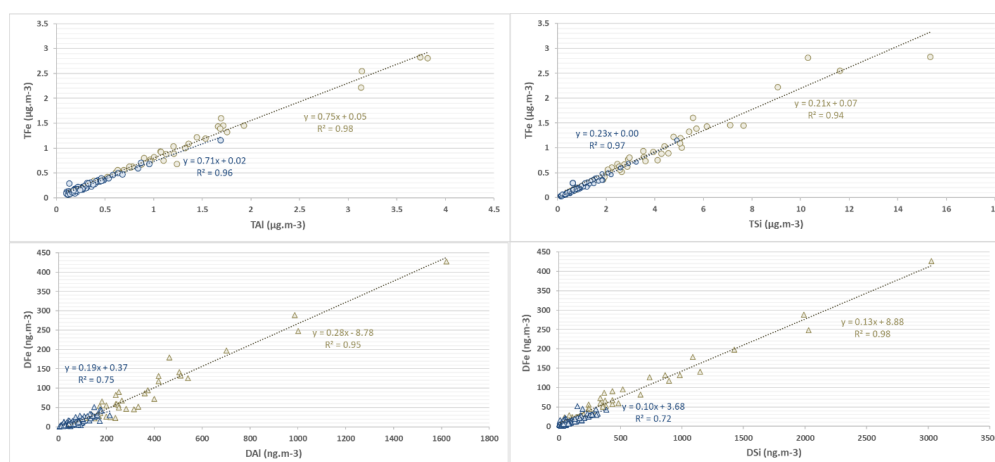
294 **Fig.2:** Temporal variability of %SFe average for dust and background samples during the different periods of
 295 sampling. In the box plots, the box indicates the interquartile range, i.e. the 25th and the 75th percentile, and
 296 the line within the box marks the median. The whiskers indicate the quartiles ± 1.5 times the interquartile range.
 297 Points above and below the whiskers indicate outliers outside the 10th and 90th percentile.



298

299 The temporal variability is similar during dust and background conditions. The highest %SFe occurred
 300 during austral spring (October-November), and in particular during episode Dust 11 from 13 to 20
 301 November 2017, when the average %SFe reached 13.8 %. The %SFe was quite similar along the
 302 year between dust and background, except between 13-20 November where the iron solubilities dur-
 303 ing Dust 11 event was very superior to the one of background samples, and to a lesser extent, in
 304 September (Dust 09) and December (Dust 13).

305 **Fig. 3** represents the correlations of Fe with Al and Si, both for the total and the dissolved concentra-
 306 tions.



307

308 **Fig. 3.** Scatterplot of TFe with respect to TAI and TSi (top panels) and DFe with respect to DAI and DSi (bot-
 309 tom panels) for dust (sand dots and triangles) and background events (blue dots and triangles). The Pearson
 310 coefficient are shown for both.

311

312 For both dust and background samples, the total Fe concentration is linearly correlated with total Al
 313 ($R^2=0.98$ and 0.96 , slope= 0.75 and 0.71 , for dust and background conditions respectively) and total
 314 Si ($R^2=0.94$ and 0.97 , slope= 0.21 and 0.23 , respectively). The slopes are consistent with typical Fe/Al
 315 and Fe/Si ratios found in desert dust from northern Africa (Formenti et al., 2014; Shelley et al., 2014),
 316 confirming the main crustal origin of Fe during all the sampling periods. Likewise, the concentrations
 317 of dissolved iron (DFe) show a strong linear correlation with both DAI and DSi, for both for dust and
 318 background events ($R^2=0.96$ and 0.75 with respect to DAI and $R^2=0.98$ and 0.73 with respect to DSi).
 319 The slopes for Al and Si are also comparable (0.19 and 0.28 for DAI and 0.10 and 0.13 for DSi,
 320 respectively in dust and in background events). A very strong linear correlation was also observed
 321 between DFe and DTi ($R^2=0.96$ and 0.84 ; not shown), another unique marker of mineral dust. Signifi-
 322 cant correlations of soluble concentrations for several elements associated with mineral dust (Fe, Al,



323 Si, Ti) have been previously obtained in remote aerosols over ocean area (Baker et al., 2016). Addi-
324 tionally, DFe during dust events correlate very closely with F^- ($R^2=0.94$, not shown), which has been
325 indicated by KL20 as being emitted in the atmosphere by the wind erosion as well as the labouring of
326 the Namibia soil, rich in fluoride mineral deposits.

327

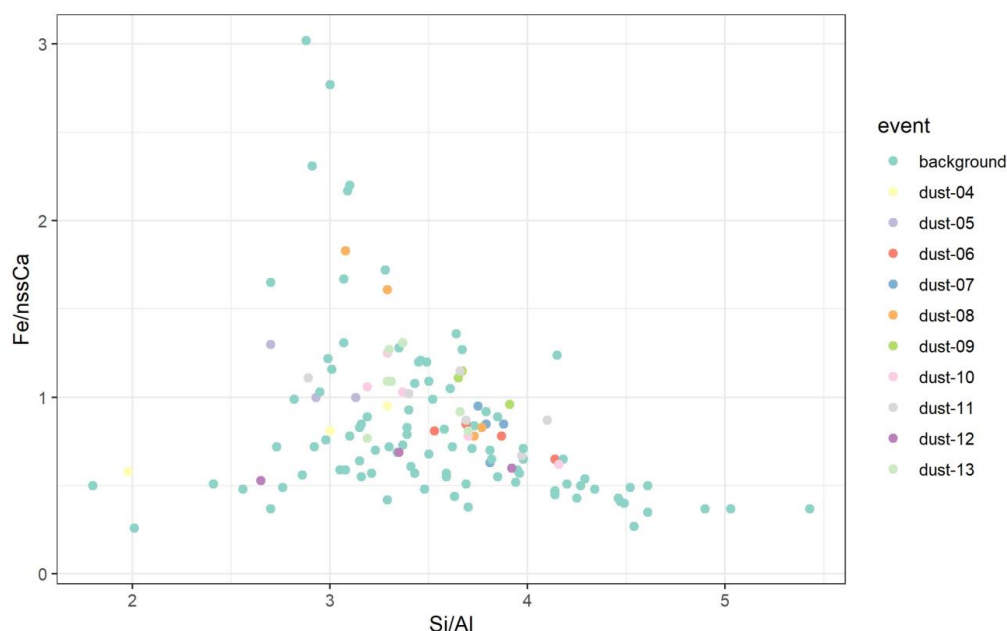
328 **4. Discussion**

329 Several studies have showed that variations in aerosol Fe solubility could result from the source/com-
330 position of the aerosols. As a matter of fact, the Fe solubility has been linked to the iron mineralogy
331 (Journet et al., 2008) and has been shown being lower for African crustal sources than in continen-
332 tal/anthropogenic sources (Desboeufs et al., 2005; Sholkovitz et al., 2009; Shelley et al., 2018). The
333 iron fractional solubility in mineral dust is also affected by source mixing (Paris et al., 2010; Desboeufs
334 et al., 2005), by (photo)chemical processing with acids or organic ligands during atmospheric
335 transport (Paris et al., 2011, Paris et Desboeufs, 2013; Wozniak et al., 2013; Swan and Ivey, 2021)
336 and by the increase of surface area to volume ratio due to size changes during transport (Baker &
337 Jickells, 2006; Marcotte et al., 2020).

338 In the following sections, we discuss these possible factors to explain the seasonality and the ex-
339 tended range of variability of the fraction Fe solubility in HBAO samples. The possible increase of
340 surface area to volume ratio during transport (Baker and Jickells, 2006; Marcotte et al., 2020) will not
341 be discussed because of lack of appropriate observations of the size distribution. Because of the
342 similar transport time suggested by back trajectories (Fig.S1), it is likely that particle size distribution
343 would be similar from one event to the other.

344 **4.1. Influence of dust composition**

345 Close to dust source, iron solubility could be mainly conditioned by the mineralogical composition of
346 dust (Journet et al., 2008, Formenti et al., 2014). Considering that soluble Fe-bearing aerosols were
347 issued from mineral dust for all the samples, the seasonality of dust emission sources (see 3.1) could
348 be a factor explaining the seasonality of %SFe (and other elements associated to mineral dust). **Fig.**
349 **4** shows the scatter plot of the elemental mass ratio of $Fe/nss-Ca^{2+}$ and Si/Al, previously used for
350 northern Africa dust to distinguish aerosol dust from source areas enriched in clays or iron oxides to
351 soils rich in quartz or carbonates (Formenti et al., 2014). Specific to Namibia, because of the strong
352 link between $nss-Ca^{2+}$ and fluorine, the $Fe/nss-Ca^{2+}$ ratio may also distinguish dust influenced by
353 fluor spar mining.



354
 355 **Fig 4.** Scatterplot of $Fe/nss-Ca^{2+}$ and Si/Al mass ratios for the samples collected at HBAO in period May-De-
 356 cember 2017. Values obtained for samples collected during the dust events are represented as brown dots.
 357 Values for samples collected outside those events (background) are represented as blue dots.
 358

359 Figure 4 indicates that the range of variability of both $Fe/nss-Ca^{2+}$ and Si/Al ratios is small when con-
 360 sidering dust events only. The elemental ratios of samples collected during the background periods
 361 are rather similar to dust events during a same sampling period, except for Si/Al for the period be-
 362 tween 19-26 May and for $Fe/nss-Ca^{2+}$ for the samples of 18-25 September, when significant differ-
 363 ences, not really explicable and not inducing a significant difference in the %SFe values are observed
 364 (**Fig. S3**).

365 The values for ambient dust measured at HBAO are consistent with those of the previous field obser-
 366 vations in Namibia (Annegarn et al., 1983; Eltayeb et al., 1993), but also with values reported by
 367 Caponi et al. (2017) for laboratory-aerosolised dust from two soils collected on the Namibian gravel
 368 plains. This is in agreement of the indications of the emission maps (**Fig. S1**), showing significant
 369 emissions in the gravel plains. The absence of seasonal cycle in the elemental composition illustrated
 370 in **Fig. S3** suggests that the seasonal change from northern to southern sources does not induce a
 371 change in the composition of the aerosol dust sampled at HBAO, which is consistent with the fact that
 372 the northern and the southern gravel plains of Namibia have similar mineralogy (Heine and Vökel,
 373 2010). This suggests that the mineralogical composition of mineral dust should not be a discriminating
 374 factor explaining the seasonality of the iron solubility observed at HBAO.



375 **4.2. Evidence of processing by marine biogenic emissions**

376 The atmospheric (in-cloud) processing associated with secondary aerosol production may increase
 377 the fractional solubility of Fe during transport (Takahashi et al., 2011; Rodríguez et al., 2021). This
 378 has also been shown for Al and Ti (Baker et al., 2020). The chemical processing could include both
 379 acidic and ligand-promoted dissolution (Desboeufs et al., 2001, Longo et al., 2016, Tao et al., 2019).
 380 Oxalic acid has previously been used as a proxy for organic ligand-mediated iron dissolution pro-
 381 cesses because it is the most abundant species in the atmosphere and is the most effective ligand in
 382 promoting iron dissolution (Baker et al., 2020; Hamilton et al., 2021). However, several secondary
 383 compounds, such as carboxylate ligands and marine secondary products derived from dimethyl sul-
 384 fide (DMS) oxidation, have been identified as playing a role in increasing the solubility fraction of iron
 385 from mineral aerosols (Johansen and Key, 2006; Paris et al., 2011; Paris and Desboeufs, 2013; Woz-
 386 niak et al., 2013 and 2015). The increase of ligands-promoted dissolution is attributed to photochem-
 387 ical reduction of Fe(III) in Fe (II) (Siefert et al., 1994; Johansen and Key, 2006).

388 To investigate these aspects, the mass concentrations of the ionic compounds (oxalate, formate,
 389 MSA, NO_3^- , NH_4^+ and nss-SO_4^{2-}) implied in the secondary aerosol production, measured at HBAO
 390 during dust and background periods are reported in **Table 3**.

391

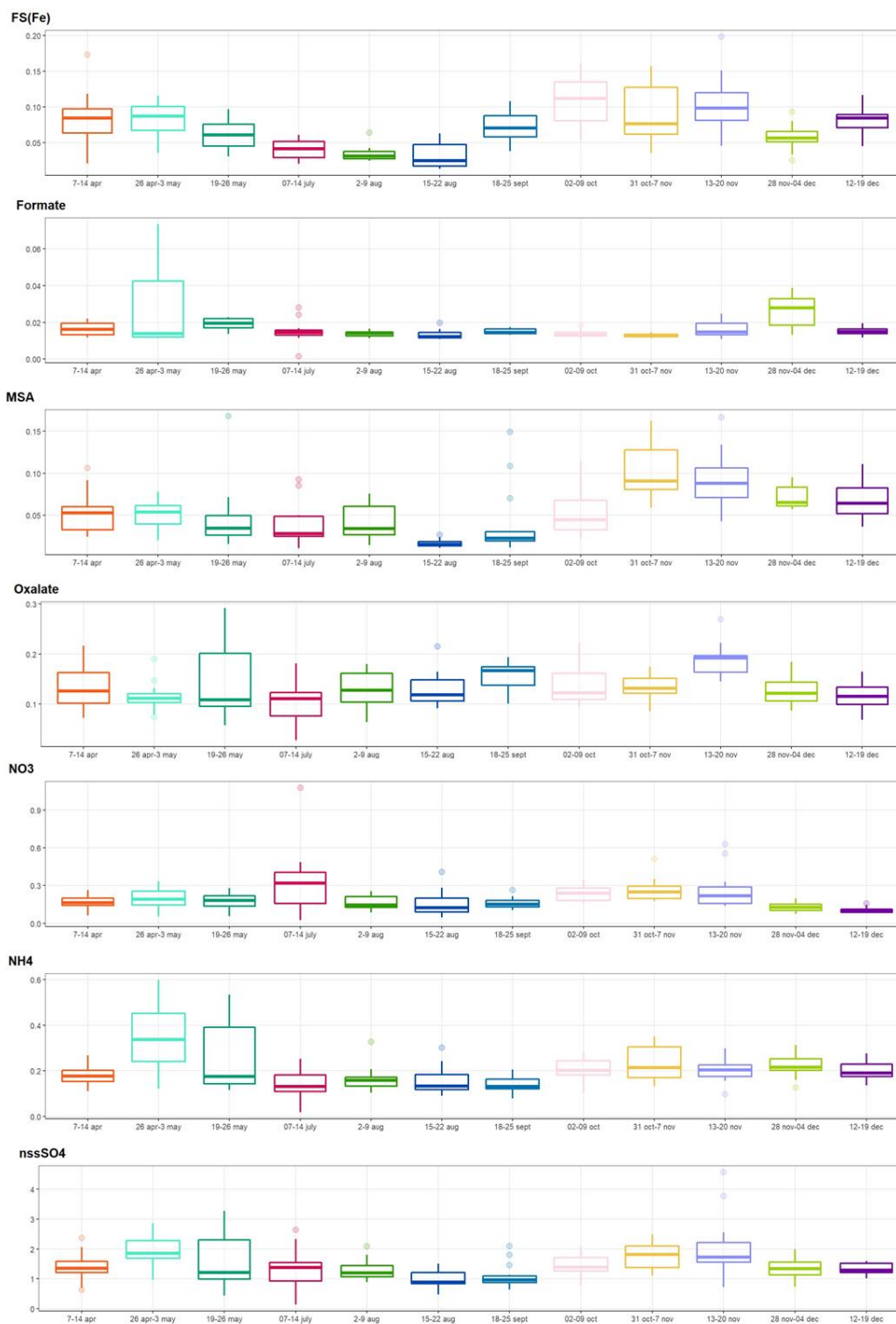
392 **Table 3.** Average and standard deviations of mass concentrations of water-soluble ions measured at HBAO during dust and
 393 background events from May to December 2017. Concentrations are expressed in ng m^{-3} . The number of samples pertaining
 394 to each occurrence is indicated in brackets.

	Dust	Background
nss-SO_4^{2-}	1795 ± 762 (N = 42)	1366 ± 505 (N=132)
Oxalate	155 ± 53 (N = 42)	127 ± 35 (N = 132)
Formate	18 ± 6 (N = 40)	16 ± 9 (N = 105)
MSA	64 ± 37 (N=36)	56 ± 36 (N=114)
NO_3^-	205 ± 79 (N=42)	200 ± 138 (N=132)
NH_4^+	192 ± 71 (N=42)	207 ± 98 (N=132)

395

396 Oxalate was the most abundant organic compound, followed by MSA, a secondary product of DMS
 397 oxidation and a unique particulate tracer of the primary marine biogenic activity (Andreae et al., 1995).
 398 On average, organic compounds were equally concentrated in dust and background events. Amongst
 399 inorganic species, nss-SO_4^{2-} was the most concentrated compound, with higher values during the
 400 dust events than during the background period.

401 Their detailed time series are shown in **Fig 5**, where it is compared to that of the iron fractional solu-
 402 bility.



403

404

405

Fig. 5. Box-plots of the averages of %SFe and secondary organic and inorganic compounds mass concentrations ($\mu\text{g m}^{-3}$) for the sampling periods including all the samples (dust + background). Boxes and whiskers as in Fig. 2.

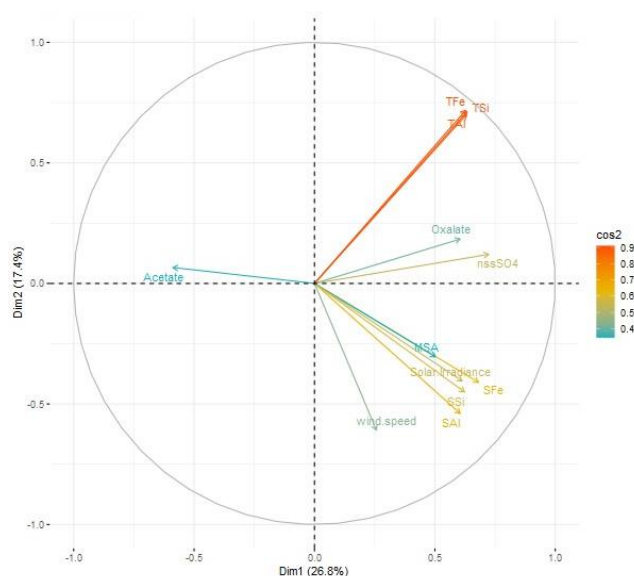


406

407 There is no clear seasonal cycle for any of the ionic compounds, with the exception of MSA, which
 408 shows a similar time variability than %SFe. MSA concentrations were lowest between May and Au-
 409 gust (average $38.0 \pm 28.0 \text{ ng m}^{-3}$), while higher concentrations were measured from September to
 410 December ($72.7 \pm 38.1 \text{ ng m}^{-3}$). These differences are also observed for the dust cases only. The
 411 average MSA concentration was $40.6 \pm 23.4 \text{ ng m}^{-3}$ for Dust 04 to Dust 08 episodes. It increased to
 412 $77.7 \pm 35.3 \text{ ng m}^{-3}$, almost a factor of 2 between episodes Dust 09 and Dust 13. The mass concen-
 413 trations and the seasonal cycle of MSA are related with the proximity of the strong coastal upwelling
 414 by the Benguela current (Formenti et al., 2019; KL20). The maximum concentration of MSA (106.2 ng m^{-3})
 415 was measured during episode Dust 11, which is also the time of the highest SFe% observa-
 416 tion. This episode was also characterised by the highest oxalate, nss-SO_4^{2-} and NO_3^- concentrations.

417 Based on their temporal variability, Fig. 6 shows the correlation plot between total Fe, Al and Si, and
 418 their respective fractional solubility, the measured secondary compounds and the meteorological condi-
 419 tions during sampling obtained from Principal Component Analysis (PCA) for all the samples. The
 420 variables correlated in time are grouped together (the closer they are to the circle, the stronger the
 421 correlation) whereas the variables which are anti-correlated are situated on the opposite side of the
 422 plot origin.

423



424 **Fig 6.** PCA analysis performed from the database including %SX and secondary ions concentrations. The scale(\cos^2)
 425 gives the factor of correlation between the different parameters. Formate, nitrate and ammonium are not visible in the plot
 426 showing that they are not correlated with the other parameters.



427

428 The PCA correlation emphasizes the dependence between %SFe (%SAI and %SSi) and the MSA
429 concentrations (correlation factor around 0.4), while indicating a weak dependence on oxalate, ace-
430 tate and nss-SO₄²⁻. Fig. 6 also shows that %SFe is correlated with both the wind speed and solar
431 irradiance (correlation factor higher than 0.6). While it is expected that the emission of mineral dust
432 occurs when the wind speed is high, the correlation of %SFe with wind speed is rather surprising as
433 both Table 1 and Fig.2 show that the %SFe is independent of the dust load. **Fig. S4** in the supple-
434 mentary material shows that the wind speed is also correlated with the MSA concentrations. This is
435 consistent with Andreae et al. (1995), who demonstrated how, in this area due to persistent phyto-
436 plankton bloom, the atmospheric concentrations of dimethylsulphide (DMS), the gaseous precursors
437 of MSA, depend on the sea-to-air flux, in turn is determined by the concentrations in the ocean water
438 and the surface wind speed. On the other hand, the MSA concentrations do not correlate significantly
439 with the average solar irradiance.

440 As previously mentioned, Johansen and Key (2006) showed an increase of dissolution of ferrihydrite,
441 a proxy of iron(oxy)hydroxide found in desert mineral dust, by photolysis of the Fe(III)-MSIA (me-
442 thanesulfinic acid) complex, producing MSA and soluble Fe. Zhuang et al. (1992) proposed an in-
443 crease of iron dissolution by the acidification of aerosol particles associated with dimethylsulphide
444 (DMS) oxidation. Here, the link between the Fe fractional solubility, solar irradiance and MSA is in
445 agreement with the photo-reduction dissolution of Fe by MSA condensation on Fe-bearing dust. Thus,
446 we attribute the iron fractional solubility seasonality observed at HBAO both to solar irradiance and
447 MSA temporal evolution via this process.

448 **4.3. Link to other sources of iron and oxalate**

449 The mass apportionment of iron reported by KL20 indicates that, during the dust events and the
450 background periods, respectively, 7% and 29% of the mass of total elemental Fe was not associated
451 to mineral dust, but rather to a factor indicated as “ammonium-neutralised component”, mostly char-
452 acterised by secondary species, and non-sea-salt potassium (nss-K⁺). Because of this association,
453 previously reported by Andreae (1983), the “ammonium-neutralised component” was associated to
454 photo-oxidation of marine biogenic emission but also episodically to biomass burning, which can be
455 transported to HBAO during the Austral summertime, when the airflow becomes anti-cyclonic, and
456 the transport of air masses laden with light absorbing aerosols has been documented (Formenti et
457 al., 2018).

458 However, our data do not indicate any significant dependence of %SFe to the percent mass fraction
459 of iron attributed to sources other than dust, notably combustion particles, which was expected in the
460 light of previous research (e.g. Desboeufs et al., 2005; Sholkovitz et al., 2009; Shelley et al., 2018;



461 Ito et al., 2021), and indeed the lowest Fe solubility (< 5%) was measured in July and August 2017,
462 when the contribution of polluted air masses should be highest.

463 The “ammonium-neutralised component” identified by KL20 included oxalate, the most concentrated
464 organic species at HBAO, and the strongest of the organic ligands promoting the photo-reduction of
465 iron in mineral dust, henceforth the increase of its fractional solubility (Paris and Desboeufs, 2013).
466 Surprisingly, excepted individual cases (Dust 13), our analysis does not show this strong link (Fig. 6),
467 which we explain by the fact that, contrary to the SFe%, the oxalate concentrations measured at
468 HBAO was practically constant with time, the possible pathways of oxalate formation in this complex
469 atmosphere being numerous and occurring through the year, from natural and anthropogenic sources
470 (marine, heavy-oil combustion, biomass burning) and in-cloud and photo-oxidative processes (Ba-
471 boukas et al., 2000; Myriokefalitakis et al., 2011).

472

473 **5. Conclusive remarks**

474 For the first time, the fractional solubility of Fe in airborne atmospheric aerosols smaller than 10 µm
475 in diameter is investigated along the west coast of Namibia, in southern Africa, a critical region for the
476 global climate.

477 Ten intense episodes of transport of mineral dust from aeolian erosion were identified from the anal-
478 ysis of aerosol samples collected between May and December 2017 at the Henties Bay Aerosol Ob-
479 servatory (HBAO). Based on modelling and measurements, source regions were identified both in the
480 northern and southern gravel plains. Our data do not provide any evidence of the possible contribution
481 of dust from coastal riverbeds, which are considered to be frequent sources of atmospheric dust and
482 soluble iron in the region. (Vickery et al., 2013; Von Holdt et al., 2017; Dansie et al., 2017a; 2017b).

483 Our first measurement indicate that the total iron represents, on average, 5.8 % (\pm 0.6 %) of the total
484 dust mass, and that the average iron fractional solubility is 6.9 % (\pm 3.3 %). These values should be
485 useful to atmospheric models estimating the dust-borne input of soluble Fe from the gravel plains in
486 Namibia to the surrounding oceans.

487 The measured iron fractional solubility is comparable to values reported from shipborne measure-
488 ments of transported dust in the remote southern oceanic regions (Baker et al., 2013; Chance et al.,
489 2015, Gao et al., 2013) but significantly higher than obtained in a benchmark laboratory evaluation
490 from the same soils and an identical dissolution protocol (*unpublished data*). The time series of frac-
491 tional solubility of Fe shows an apparent seasonal cycle which is independent of dust composition.
492 This is also the case for Al and Si.



493 The observations presented in this paper exclude a major role of sources other than mineral dust to
494 play on the values and the variability of %SFe, which might be due to the location of our sampling
495 site, remote and only occasionally affected by polluted air masses (Formenti et al., 2018).

496 Conversely, the seasonal increase of the iron fractional solubility is associated to that of the concen-
497 trations of MSA and correlated to meteorological parameters such as the wind speed and the surface
498 solar irradiance. Our observations support the role of photo-chemical processes in the dissolution of
499 Fe in our samples, and suggest that the oxidation of the marine biogenic emissions from the northern
500 Benguela upwelling, favoured under high wind speed conditions, could play a significant role in in-
501 creasing the solubility of elemental iron in mineral dust aerosols over coastal Namibian. This is in
502 agreement with the mechanism described by Zhuang et al. (1992), who proposed an increase of iron
503 dissolution by the acidification of aerosol particles associated with DMS oxidation, and Johansen and
504 Key (2006), who showed an increase of dissolution of ferrihydrite, a proxy of iron(oxy)hydroxide found
505 in desert mineral dust, by photolysis of the Fe(III)-MSIA (methanesulfinic acid) complex, producing
506 MSA and soluble Fe. It is interesting to note that due to the high correlation between %SFe and %SAI
507 and %SSi, the photochemical processes could also impact the solubility of all element-bearing dust.
508 The possible mechanism suggested by this paper could be responsible for initiating a feedback loop
509 whereby the input of dust of increased solubility would result in stronger marine biogenic emissions
510 to the atmosphere.

511 In conclusion, this paper describes the very first field observations suggesting that, while airborne,
512 the atmospheric iron from mineral dust experiences a complex and dynamic environment where the
513 interplay between the input of atmospheric iron from transported dust and the marine biogenic emis-
514 sions from the Benguela oceanic upwelling system should be further addressed by future research.
515 This possible mechanism could increase the iron solubility in mineral dust, maybe also initiating a
516 feedback loop whereby the input of dust of increased solubility would result in stronger marine bio-
517 genic emissions to the atmosphere. Beside sulphur species, the role of Volatile Organic Compounds
518 (VOCs), in particular butene, massively emitted by the organisms in the coastal marine foam (Giorio
519 et al., 2022), should also be explored.

520

521 **Data availability.** Original and analysed data are available at the AERIS (<https://aeroclo.aeris->
522 [data.fr/project/](https://aeroclo.aeris-data.fr/project/), last accessed 20/07/2023). The statistical FactoMineR package is available in R (R
523 version 4.1.2, 2021; http://factominer.free.fr/index_fr.html, last accessed 20/07/2023). Meteorological
524 data from the Wlotzkasbaken station (22.31°S, 14.45°E, 73 m asl) are part of the Southern African
525 Science Service Centre for Climate Change and Adaptive Land Management (SASSCAL) Observa-
526 tionNet (<https://www.sasscal.org/>; last accessed 14/04/2023).

527



528 **Author contributions.** PF, DK, SJP, AN, MC, AF and SC prepared and performed the filter sampling.
529 RT, KD, PF, SC, and CMB performed the XRF, IC and ICP analysis of the collected samples. KS and
530 SF performed the model calculations of dust emission fluxes. JPC performed the model calculations
531 of air mass back-trajectories. HA and JC provided with the satellite retrieval of fog and low clouds.
532 PF, KD, RT and SJP analysed and interpreted the dataset. PF and KD wrote the paper with contribu-
533 tions from RT and SJP, and the remaining authors. PF and SJP provided funding. PF coordinated the
534 research activity and supervised its planning and execution.

535

536 **Competing interests.** PF is guest editor for the ACP Special Issue “New observations and related
537 modelling studies of the aerosol–cloud–climate system in the Southeast Atlantic and southern Africa
538 regions”. The remaining authors declare that they have no conflicts of interests.

539

540 **Special issue statement.** This article is part of the special issue “New observations and related mod-
541 elling studies of the aerosol–cloud–climate system in the Southeast Atlantic and southern Africa re-
542 gions (ACP/AMT inter-journal SI)”. It is not associated with a conference.

543

544 **Acknowledgements.** This work receives funding by the French Centre National de la Recherche
545 Scientifique (CNRS) and the South African National Research Foundation (NRF) through the
546 “Groupement de Recherche Internationale Atmospheric Research in southern Africa and the Indian
547 Ocean” (GDRI-ARSAIO) and the Project International de Coopération Scientifique (PICS) “Long-term
548 observations of aerosol properties in Southern Africa” (contract n. 260888) as well as by the Part-
549 nariats Hubert Curien (PHC) PROTEA of the French Minister of Foreign Affairs and International De-
550 velopment (contract numbers 33913SF and 38255ZE). D. Klopper acknowledges the financial support
551 of the Climatology Research Group of North-West University and the travel scholarship of the French
552 Embassy in South Africa (internship at LISA in summer 2018). R. Torres-Sánchez acknowledges the
553 Postdoctoral Fellowship Margarita Alsolas (University of Huelva) funded by the Ministry of Universities
554 of Spain (NextGenerationEU). The Southern African Science Service Centre for Climate Change and
555 Adaptive Land Management (SASSCAL) ObservationNet (<https://www.sasscal.org/>) is acknowledged
556 for open-access data provision. The authors would also like to acknowledge the support by the IPGP
557 platform PARI for HR-ICP-MS analysis. F. Lahmidi and Z. Zeng (LISA) are acknowledged for support
558 to the ion chromatography analysis.

559



560 **References**

- 561 Andersen, H. and Cermak, J.: First fully diurnal fog and low cloud satellite detection reveals life cycle in the
562 Namib, *Atmos. Meas. Tech.*, 11, 5461–5470, doi: 10.5194/amt-11-5461-2018, 2018.
- 563 Andersen, H., Cermak, J., Solodovnik, I., Lelli, L. and Vogt, R.: Spatiotemporal dynamics of fog and low clouds
564 in the Namib unveiled with ground- and space-based observations, *Atmos. Chem. Phys.*, 1, 4383–4392, doi:
565 10.5194/acp-19-4383-2019, 2019.
- 566 Andersen, H., Cermak, J., Fuchs, J., Knippertz, P., Gaetani, M., Quinting, J., Sippel, S., and Vogt, R.: Synoptic-
567 scale controls of fog and low-cloud variability in the Namib Desert, *Atmos. Chem. Phys.*, 20, 3415–3438,
568 <https://doi.org/10.5194/acp-20-3415-2020>, 2020.
- 569 Andreae, M. O.: Soot Carbon and Excess Fine Potassium: Long-Range Transport of Combustion-Derived Aer-
570 osols, *Science*, 220, 1148–1151, doi:10.1126/science.220.4602.1148, 1983.
- 571 Andreae, M. O., Elbert, W., and de Mora, S. J.: Biogenic sulfur emissions and aerosols over the tropical South
572 Atlantic: 3. Atmospheric dimethylsulfide, aerosols and cloud condensation nuclei, *J. Geophys. Res.*, 100,
573 11335–11356, <https://doi.org/10.1029/94JD02828>, 1995.
- 574 Annegarn, H.J., van Grieken, R.E., Bibby, D.M. and von Blottnitz, F.: Background Aerosol Composition in the
575 Namib Desert, South West Africa (Namibia), *Atmos. Environ.*, 17, 2045–2053, doi: 10.1016/0004-
576 6981(83)90361-X, 1983.
- 577 Bhattachan, A., D'Odorico, P., Baddock, M.C., Zobeck, T.M., Okin, G.S., Cassar, N.: The Southern Kalahari: a
578 potential new dust source in the Southern hemisphere?, *Environ. Res. Lett.*, 7, 024001.
579 <http://dx.doi.org/10.1088/1748-9326/7/2/024001>, 2012.
- 580 Bhattachan, A., P. D'Odorico, and G. S. Okin, Biogeochemistry of dust sources in Southern Africa, *J. Arid En-
581 viron.*, 117, 18–27, <http://dx.doi.org/10.1016/j.jaridenv.2015.02.013>, 2015.
- 582 Baboukas, E. D., Kanakidou, M., and Mihalopoulos, N.: Carboxylic acids in gas and particulate phase above
583 the Atlantic Ocean, *J. Geophys. Res.*, 105, 14459–14471, <https://doi.org/10.1029/1999JD900977>, 2000.
- 584 Baker A.R., T. D. Jickells, M. Witt, and K. L. Linge, Trends in the solubility of iron, aluminium, manganese and
585 phosphorus in aerosol collected over the Atlantic Ocean., *Marine Chem.*, 98, 43–58,
586 <https://doi.org/10.1016/j.marchem.2005.06.004>, 2006.
- 587 Baker, A. R., and T. D. Jickells, Mineral particle size as a control on aerosol iron solubility, *Geophys. Res. Lett.*,
588 33, L17608. <https://doi.org/10.1029/2006GL026557>, 2006.
- 589 Baker, A. R., C. Adams C., T. G. Bell, T. D. Jickells, and L. Ganzeveld, Estimation of atmospheric nutrient inputs
590 to the Atlantic Ocean from 50°N to 50°S based on large-scale field sampling: iron and other dust-associated
591 elements, *Glob. Biogeochem. Cycles*, 27, 755–767, doi:10.1002/gbc.20062, 2013.
- 592 Baker, A. R., M. Thomas, H. W. Bange, and E. Plasencia Sánchez, E., Soluble trace metals in aerosols over
593 the tropical south-east Pacific offshore of Peru, *Biogeosciences*, 13, 817–825, [https://doi.org/10.5194/bg-13-
594 817-2016](https://doi.org/10.5194/bg-13-817-2016), 2016.



- 595 Baker, Alex R., et T. D. Jickells, Atmospheric deposition of soluble trace elements along the Atlantic Meridional
596 Transect (AMT), in *The Atlantic Meridional Transect programme (1995-2016)* 158: 41-51.
597 <https://doi.org/10.1016/j.pocean.2016.10.002>, 2017.
- 598 Baker, A. R., M. Li, and R. Chance, Trace metal fractional solubility in size-segregated aerosols from the tropical
599 eastern Atlantic Ocean, *Global Biogeochemical Cycles*, 34, e2019GB006510.
600 <https://doi.org/10.1029/2019GB006510>, 2020.
- 601 Bryant, R. G., Bigg, G. R., Mahowald, N. M., Eckardt, F. D., and Ross, S. G., Dust emission response to climate
602 in southern Africa, *J. Geophys. Res.*, 112, D09207, doi:10.1029/2005JD007025, 2007.
- 603 Caponi, L., Formenti, P., Massabó, D., Di Biagio, C., Cazaunau, M., Pangui, E., Chevaillier, S., Landrot, G.,
604 Andreae, M. O., Kandler, K., Piketh, S., Saeed, T., Seibert, D., Williams, E., Balkanski, Y., Prati, P., and
605 Doussin, J.-F.: Spectral- and size-resolved mass absorption efficiency of mineral dust aerosols in the
606 shortwave spectrum: a simulation chamber study, *Atmos. Chem. Phys.*, 17, 7175–7191,
607 <https://doi.org/10.5194/acp-17-7175-2017>, 2017.
- 608 Chaboureau, J.-P., L. Labbouz, C. Flamant, and A. Hodzic. Acceleration of the southern African easterly jet
609 driven by radiative effect of biomass burning aerosols and its impact on transport during AEROCLO-sA, *At-
610 mos. Chem. Phys.*, 22, 8639-8658, <https://doi.org/10.5194/acp-22-8639-2022>, 2022.
- 611 Chance R, T. D. Jickells and A. R. Baker, Atmospheric trace metal concentrations, solubility and deposition
612 fluxes in remote marine air over the south-east Atlantic, *Marine Chemistry*, 177, 45–56, doi:10.1016/j.mar-
613 chem.2015.06.028, 2015.
- 614 Dansie, A. P., G. F. S. Wiggs, D. S. G. Thomas, and R. Washington, Measurements of windblown dust charac-
615 teristics and ocean fertilisation potential: The ephemeral river valleys of Namibia, *Aeolian Res.*, 29, 30–41,
616 doi:10.1016/j.aeolia.2017.08.002, 2017a.
- 617 Dansie, A. P., G. F. S. Wiggs, and D. S. G. Thomas, Iron and nutrient content of wind-erodible sediment in the
618 ephemeral river valleys of Namibia, *Geomorphology*, 290, 335-346, <https://doi.org/10.1016/j.geomorph.2017.03.016>, 2017b.
- 620 Dansie AP, Thomas DSG, Wiggs GFS, Baddock MC, Ashpole I. Plumes and blooms - Locally-sourced Fe-rich
621 aeolian mineral dust drives phytoplankton growth off southwest Africa. *Sci Total Environ.*, doi: 10.1016/j.sci-
622 totenv.2022.154562, 2022.
- 623 Desboeufs, K. V., R. Losno, et J. L. Colin, Factors influencing aerosol solubility during cloud processes, *Atmos.*
624 *Environ.*, 35, 3529-3537, [https://doi.org/10.1016/S1352-2310\(00\)00472-6](https://doi.org/10.1016/S1352-2310(00)00472-6), 2001.
- 625 Desboeufs, K.V., Sofikitis, A., Losno, R., Colin, J.L., Ausset, P. Dissolution and solubility of trace metals from
626 natural and anthropogenic aerosol particulate matter, *Chemosphere* 58, 195–203, 2005.
- 627 Desboeufs, K., Fu, Y., Bressac, M., Tovar-Sánchez, A., Triquet, S., Doussin, J.F., Giorio, C., Chazette, P.,
628 Disnaquet, J., Feron, A., Formenti, P., Maisonneuve, F., Rodríguez-Romero, A., Zapf, P., Dulac, F., and
629 Guieu, C., Wet deposition in the remote western and central Mediterranean as a source of trace metals to
630 surface seawater, *Atmos. Chem. Phys.*, 22, 2309–2332, <https://doi.org/10.5194/acp-22-2309-2022>, 2022.



- 631 Eltayeb, M.A.; Van Grieken, R.E., Maenhaut, W. and Annegarn, H.J.: Aerosol-Soil Fractionation for Namib De-
632 sert Samples. *Atmos. Environ.*, 27(5), [https://doi.org/10.1016/0960-1686\(93\)90185-2](https://doi.org/10.1016/0960-1686(93)90185-2), 1993.
- 633 Feuerstein, S., and Schepanski, K.: Identification of Dust Sources in a Saharan Dust Hot-Spot and Their Imple-
634 mentation in a Dust-Emission Model, *Remote Sensing*, 11, doi:10.3390/rs110100004, 2019.
- 635 Flamant, C., M. Gaetani, J.-P. Chaboureaud, P. Chazette, S. J. Piketh, and P. Formenti. Smoke in the river: an
636 Aerosols, Radiation and Clouds in southern Africa (AEROCLO-sA) case study, *Atmos. Chem. Phys.*, 22,
637 5701–5724, <https://doi.org/10.5194/acp-22-5701-2022>, 2022.
- 638 Formenti, P., S. Caqueneau, K. Desboeufs, A. Klaver, S. Chevaillier, E. Journet, J. L. Rajot, Mapping the phys-
639 ico-chemical properties of mineral dust in western Africa: mineralogical composition, *Atmos. Chem. Phys.*, 14,
640 10663-1068, 2014.
- 641 Formenti, P., Piketh, S. J., Namwoonde, A., Klopper, D., Burger, R., Cazaunau, M., Feron, A., Gaimoz, C.,
642 Broccardo, S., Walton, N., Desboeufs, K., Siour, G., Hanghome, M., Mafwila, S., Omeregje, E., Junkermann,
643 W., and Maenhaut, W.: Three years of measurements of light-absorbing aerosols over coastal Namibia: sea-
644 sonality, origin, and transport, *Atmos. Chem. Phys.*, 18, 17003-17016, [https://doi.org/10.5194/acp-18-17003-](https://doi.org/10.5194/acp-18-17003-2018)
645 2018, 2018.
- 646 Formenti, P., B. D'Anna, C. Flamant, M. Mallet, S.J. Piketh, K. Schepanski, F. Waquet, F. Auriol, G. Brogniez,
647 F. Burnet, J. Chaboureaud, A. Chauvigné, P. Chazette, C. Denjean, K. Desboeufs, J. Doussin, N. Elguindi, S.
648 Feuerstein, M. Gaetani, C. Giorio, D. Klopper, M.D. Mallet, P. Nabat, A. Monod, F. Solmon, A. Namwoonde,
649 C. Chikwililwa, R. Mushi, E.J. Welton, and B. Holben, The Aerosols, Radiation and Clouds in Southern Africa
650 Field Campaign in Namibia: Overview, Illustrative Observations, and Way Forward, *Bull. Amer. Meteor. Soc.*,
651 100, 1277–1298, <https://doi.org/10.1175/BAMS-D-17-0278.1>, 2019.
- 652 Gao, Y., Xu, G., Zhan, J., Zhang, J., Li, W., Lin, Q., Chen, L., and Lin, H., Spatial and particle size distributions
653 of atmospheric dissolvable iron in aerosols and its input to the Southern Ocean and coastal East Antarctica,
654 *J. Geophys. Res.*, 118, 12,634–12,648, doi:10.1002/2013JD020367, 2013.
- 655 Gili, S., Vanderstraeten, A., Chaput, A., King, J., Gaiero, D. M., Delmonte, B., Vallelonga, Paola Formenti,
656 Claudia Di-Biagio, Mathieu Cazaunau, Edouard Pangui, Jean-Francois Doussin, Mattielli, N., South African
657 dust contribution to the high southern latitudes and East Antarctica during interglacial stages, *Communications*
658 *Earth & Environment*, 3, 129, <https://doi.org/10.1038/s43247-022-00464-z>, 2022.
- 659 Ginoux, P., Prospero, J.M., Gill, T.E., Hsu, N.C., Zhao, M.: Global-scale attribution of anthropogenic and natural
660 dust sources and their emission rates based on MODIS Deep Blue aerosols products, *Rev. Geophys.*, 50,
661 RG3005, doi:10.1029/2012RG000388, 2012.
- 662 Giorio, C., Doussin, J.F., D'Anna, B., Mas, S., Filippi, D., Denjean, C., Mallet, M.D., Bourriane, T., Burnet, F.,
663 Cazaunau, M., Chikwililwa, C., Desboeufs, K., Feron, A., Michoud, V., Namwoonde, A., Andreae, M.O., Piketh,
664 S.J. and Formenti, P.: Butene emissions from coastal ecosystems may contribute to new particle formation,
665 *Geophys. Res. Lett.*, 49, <https://doi.org/10.1029/2022GL098770>, 2022.
- 666 Grini, A., Tulet, P., and Gomes, L.: Dusty weather forecasts using the MesoNH mesoscale atmospheric model.
667 *J. Geophys. Res.*, 111, D19205, <https://doi.org/10.1029/2005JD007007>, 2006.



- 668 Hamilton, D. S., Perron, M.M.G., Bond, T.C., Bowie, A.R., Buchholz, R.R., Guieu, C., Ito, A., Maenhaut, W.,
669 Myriokefalitakis, S., Olgun, N., Rathod, S.D., Schepanski, K., Tagliabue, A., Wagner, R. and Mahowald, N.M.:
670 Earth, wind, fire, and pollution: Aerosol nutrient sources and impacts on ocean biogeochemistry, Annual re-
671 view of Marine Science, 14, pp. 303- 330, <https://doi.org/10.1146/annurev-marine-031921-013612>, 2021.
- 672 Heike, K and J. Volkel, Soil clay minerals in Namibia and their significance for the terrestrial and marine past
673 global change, African Study Monographs, Suppl.40, 2010.
- 674 Heimbürger, A., Losno, R., and Triquet, S.: Solubility of iron and other trace elements in rainwater collected on
675 the Kerguelen Islands (South Indian Ocean), Biogeosciences, 10, 6617–6628, <https://doi.org/10.5194/bg-10-6617-2013>, 2013.
- 677 Hooper, H., Mayewski, P., Marx, S., Henson, S., Potocki, M., Sneed, S., Handley, M., Gasso, S., Fischer, M.,
678 Saunders, K.M., Examining links between dust deposition and phytoplankton response using ice cores. Aeol-
679 ian Res., 36, 45-60, <https://doi.org/10.1016/j.aeolia.2018.11.001>, 2019.
- 680 Ito, A., and Kok, J. F.: Do dust emissions from sparsely vegetated regions dominate atmospheric iron supply to
681 the Southern Ocean?, J. Geophys. Res., 122, 3987-4002, <https://doi.org/10.1002/2016JD025939>, 2017.
- 682 Ito, A., Y. Ye, C. Baldo, and Z. Shi, Ocean Fertilization by Pyrogenic Aerosol Iron. npj Climate Atmos. Sci., 4,
683 30, doi: 10.1038/s41612-021-00185-8, 2021.
- 684 Jickells, T., Andersen, K.K., Baker, A., Bergametti, G., Brooks, N., Cao, J., Boyd, P., Duce, R., Hunter, K.,
685 Global iron connections between desert dust, ocean biogeochemistry, and climate, Science, 308, 67-71, DOI:
686 10.1126/science.1105959, 2005.
- 687 Journet, E., Desboeufs, K., Caquineau, S. and Colin, J. L.: Mineralogy as a critical factor of dust iron solubility,
688 Geophys. Res. Lett., 35, <https://doi.org/10.1029/2007GL031589>, 2008.
- 689 Johansen, A. M., and Key, J. M.: Photoreductive dissolution of ferrihydrite by methanesulfinic acid: Evidence of
690 a direct link between dimethylsulfide and iron-bioavailability, Geophys. Res. Lett., 33, L14818,
691 doi:10.1029/2006GL026010, 2006.
- 692 Kaplan, J.O., Bigelow, N.H., Prentice, I.C., Harrison, S.P., Bartlein, P.J., Christensen, T.R., Cramer, W., Matve-
693 yeva, N.V., McGuire, A.D., Murray, D.F., Razzhivin, V.Y., Smith, B., Walker, D.A., Anderson, P.M., Andreev,
694 A.A., Brubaker, L.B., Edwards, M.E. and Lozhkin A.V.: Climate change and Arctic ecosystems: 2. Modeling,
695 paleodata-model comparison and future projections, J. Atmos. Res., 108, 8171, doi: 10.1029/2002JD002559,
696 2003.
- 697 Kanguuehi, K. I., Southern African dust characteristics and potential impacts on the surrounding oceans, PhD
698 Thesis, Stellenbosch University, <http://hdl.handle.net/10019.1/123923>, 2021.
- 699 Klopfer, D., Formenti, P., Namwoonde, A., Cazaunau, M., Chevallier, S., Feron, A., Gaimoz, C., Hease, P.,
700 Lahmidi, F., Mirande-Bret, C., Triquet, S., Zeng, Z. And Piketh, S.J.: Chemical composition and source apportionment of atmospheric aerosols on the Namibian Coast, Atmos. Chem. Phys., 20, pp. 15811 – 15833,
701 <https://doi.org/10.5194/acp-20-15811-2020>, 2020.



- 703 Kok, J. F., Albani, S., Mahowald, N. M., and Ward, D. S.: An improved dust emission model – Part 2: Evaluation
704 in the Community Earth System Model, with implications for the use of dust source functions, *Atmos. Chem.*
705 *Phys.*, 14, 13043–13061, <https://doi.org/10.5194/acp-14-13043-2014>, 2014.
- 706 Kok, J.F., Ridley, D.A., Zhou, Q., Miller, R.L., Zhao, C., Heald, C.L., Ward, D.S., Albani, S., Haustein, K.: Smaller
707 desert dust cooling effect estimated from analysis of dust size and abundance. *Nature Geoscience*, 10, 274–
708 278, <https://doi.org/10.1038/ngeo2912>, 2017.
- 709 Laurent, B., Marticorena, B., Bergametti, G., Chazette, P., Maignan, F. and Schmechtig C.: Simulation of the
710 mineral dust emission frequencies from desert areas of China and Mongolia using an aerodynamic roughness
711 length map derived from POLDER/ADEOS 1 surface products, *J. Geophys. Res.*, 110, D18, doi:
712 10.1029/2004JD005013, 2005.
- 713 Lide, D. R.: *CRC Handbook of Chemistry and Physics 1991–1992*, CRC Press, Boca Raton, Florida, 1992.
- 714 Liu, M., Matsui, H., Hamilton, D.S., Lamb, K.D., Rathod, S.D., Schwarz, J.P. and Mahowald, N.M.: The underap-
715 preciated role of anthropogenic sources in atmospheric soluble iron flux to the Southern Ocean, *Climate At-*
716 *mos. Sci.*, 5, 28, <https://doi.org/10.1038/s41612-022-00250-w>, 2022.
- 717 Longo, A., F. Y. Feng, B., W. M. Landing, R.U. Shelley, A. Nenes, N. Mihalopoulos, K. Violaki, E. D. Ingall.
718 Influence of Atmospheric Processes on the Solubility and Composition of Iron in Saharan Dust, *Environ. Sci.*
719 *Tech.*, 50, 13: 6912-20. <https://doi.org/10.1021/acs.est.6b02605>, 2016.
- 720 Mahowald, N., Luo, C., del Corral, J., Zender, C.S.: Interannual variability in atmospheric mineral aerosols from
721 a 22-year model simulation and observational data, *J. Geophys. Res.*, 108 (D12),
722 <https://doi.org/10.1029/2002JD002821>, 2003.
- 723 Marcotte, A.R., Anbar, A.D., Majestic, B.J., Herckes, P.: Mineral dust and iron solubility: Effects of composition,
724 particle size, and surface area, *Atmosphere*, 11, 533, doi:10.3390/atmos11050533, 2020.
- 725 Marticorena, B. and Bergametti, G.: Modelling the atmospheric dust cycle: 1. Design of a soil-derived dust
726 emission scheme, *J. Geochem. Res.*, 16415-16430, 1995.
- 727 Marticorena, B., Chazette, P., Bergametti, G., Dulac, F., Legrand, M.: Mapping the aerodynamic roughness
728 length of desert surfaces from the POLDER/ADEOS bi-directional reflectance product, *Int. J. Remote Sens.*,
729 25, 603– 626, 2004.
- 730 Myriokefalitakis, S., Tsigaridis, K., Mihalopoulos, N., Sciare, J., Nenes, A., Kawamura, K., Segers, A., and
731 Kanakidou, M.: In-cloud oxalate formation in the global troposphere: a 3-D modeling study, *Atmos. Chem.*
732 *Phys.*, 11, 5761-5782, doi:10.5194/acp-11-5761-2011, 2011.
- 733 Paris, R., Desboeufs, K. V., Formenti, P., Nava, S., and Chou, C.: Chemical characterisation of iron in dust and
734 biomass burning aerosols during AMMA-SOP0/DABEX: implication for iron solubility, *Atmos. Chem. Phys.*,
735 10, 4273–4282, <https://doi.org/10.5194/acp-10-4273-2010>, 2010.
- 736 Paris, R., K.V. Desboeufs, et E. Journet. Variability of dust iron solubility in atmospheric waters: Investigation of
737 the role of oxalate organic complexation, *Atmos. Environ.*, 45, 6510-17. [https://doi.org/10.1016/j.at-](https://doi.org/10.1016/j.atmosenv.2011.08.068)
738 [mosenv.2011.08.068](https://doi.org/10.1016/j.atmosenv.2011.08.068), 2011.



- 739 Paris, R., and K. V. Desboeufs, Effect of atmospheric organic complexation on iron-bearing dust solubility. *Atmos. Chem. Phys.*, 13, 4895-4905, <https://doi.org/10.5194/acp-13-4895-2013>, 2013.
- 741 Prospero, J.M., Ginoux, P., Torres, O., Nicholson S.E. and Gill, T.M.: Environmental characterization of global
742 sources of atmospheric soil dust identified with the Nimbus 7 total ozone mapping spectrometer (TOMS) ab-
743 sorbing aerosol product. *Reviews of Geophysics*, 40 (1): 1002, <https://doi.org/10.1029/2000RG000095>, 2002.
- 744 Redemann, J., Wood, R., Zuidema, P., Doherty, S. J., Luna, B., LeBlanc, S. E., Diamond, M. S., Shinozuka, Y.,
745 Chang, I. Y., Ueyama, R., Pfister, L., Ryoo, J.-M., Dobracki, A. N., da Silva, A. M., Longo, K. M., Kacenelen-
746 bogen, M. S., Flynn, C. J., Pistone, K., Knox, N. M., Piketh, S. J., Haywood, J. M., Formenti, P., Mallet, M.,
747 Stier, P., Ackerman, A. S., Bauer, S. E., Fridlind, A. M., Carmichael, G. R., Saide, P. E., Ferrada, G. A., Howell,
748 S. G., Freitag, S., Cairns, B., Holben, B. N., Knobelspiesse, K. D., Tanelli, S., L'Ecuyer, T. S., Dzambo, A. M.,
749 Sy, O. O., McFarquhar, G. M., Poellot, M. R., Gupta, S., O'Brien, J. R., Nenes, A., Kacarab, M., Wong, J. P.
750 S., Small-Griswold, J. D., Thornhill, K. L., Noone, D., Podolske, J. R., Schmidt, K. S., Pilewskie, P., Chen, H.,
751 Cochrane, S. P., Sedlacek, A. J., Lang, T. J., Stith, E., Segal-Rozenhaimer, M., Ferrare, R. A., Burton, S. P.,
752 Hostetler, C. A., Diner, D. J., Seidel, F. C., Platnick, S. E., Myers, J. S., Meyer, K. G., Spangenberg, D. A.,
753 Maring, H., and Gao, L.: An overview of the ORACLES (ObseRvations of Aerosols above CLouds and their
754 intEractionS) project: aerosol–cloud–radiation interactions in the southeast Atlantic basin, *Atmos. Chem.*
755 *Phys.*, 21, 1507–1563, <https://doi.org/10.5194/acp-21-1507-2021>, 2021.
- 756 Reichholf, J. H., Is Saharan Dust a Major Source of Nutrients for the Amazonian Rain Forest?, *Studies on*
757 *Neotropical Fauna and Environment*, 21:4, 251-255, DOI: 10.1080/01650528609360710, 1986.
- 758 Rodríguez, S., Prospero, J.M., Lopez-Darias, J., Garcia-Alvarez, M.I., Zuidema, P., Nava, S., Lucarelli, F., Gas-
759 ton, C.J., Galindo, L., Sosa, E.: Tracking the changes of iron solubility and air pollutants traces as African dust
760 transits the Atlantic in the Saharan dust outbreaks. *Atmos. Environ.*, 246, 118092, <https://doi.org/10.1016/j.atmosenv.2020.118092>, 2021.
- 762 Shelley, R.U., Morton, P.L., Landing, W.M., Elemental ratios and enrichment factors in aerosols from the US-
763 GEOTRACES North Atlantic transects. *Deep-Sea Res. II*, 2014.
- 764 Shelley, R. U., Landing, W. M., Ussher, S. J., Planquette, H., & Sarthou, G. Regional trends in the fractional
765 solubility of Fe and other metals from North Atlantic aerosols (GEOTRACES cruises GA01 and GA03) follow-
766 ing a two-stage leach, *Biogeosciences*, 15(8), 2271–2288. <https://doi.org/10.5194/bg-15-2271-2018>, 2018.
- 767 Sholkovitz, E.R., Sedwick, P.N., Church, T.M. Influence of anthropogenic combustion emissions on the deposi-
768 tion of soluble aerosol iron to the ocean: empirical estimates for island sites in the North Atlantic, *Geochim.*
769 *Cosmochim. Acta*, 73, 3981–4003, <http://dx.doi.org/10.1016/j.gca.2009.04.029>, 2009.
- 770 Siefert, R. L., S. O. Pehkonen, Y. Erel, and M. R. Hoffman, Iron photochemistry of aqueous suspensions of
771 ambient aerosol with added organic acids, *Geochim. Cosmochim. Acta*, 58, 3271–3279, 1994.
- 772 Spirig, R., Vogt, R., Larsen, J. A., Feigenwinter, C., Wicki, A., Franceschi, J., Parlow, E., Adler, B., Kalthoff, N.,
773 Cermak, J., Andersen, H., Fuchs, J., Bott, A., Hacker, M., Wagner, N., Maggs-Kölling, G., Wassenaar, T. and
774 Seely, M.: Probing the fog life-cycles in the Namib desert, *Bull. Am. Met. Soc.*, 100, 2491-2508,
775 doi:10.1175/bams-d-18-0142.1, 2019.



- 776 Swan, H.B., and J. P. Ivey, Elevated particulate methanesulfonate, oxalate and iron over Sydney Harbour in the
777 austral summer of 2019-20 during unprecedented bushfire activity, *Atmos. Environ.*, 226, 118739,
778 <https://doi.org/10.1016/j.atmosenv.2021.118739>, 2021.
- 779 Swap, R., Garstang, M., Macko, S.A., et al., The long-range transport of southern African aerosols to the tropical
780 South Atlantic. *J. Geophys. Res.*, 101, 23777–23791, <https://doi.org/10.1029/95jd01049>, 1996.
- 781 Takahashi, Y., Higashi, M., Fukurawa, T., Mitsunobu, S.: Change of iron species and iron solubility in Asian
782 dust during the long-range transport from western China to Japan, *Atmos. Chem. Phys.*, 11, 11237-11252,
783 [doi:10.5194/acp-11-11237-2011](https://doi.org/10.5194/acp-11-11237-2011), 2011.
- 784 Tao, Y., Murphy, J.G.: The mechanisms responsible for the interactions among oxalate, pH, and Fe dissolution
785 in PM_{2.5}. *Earth and Space Chemistry*, 3, 2259-2265, <https://doi.org/10.1021/acsearthspacechem.9b00172>,
786 2019.
- 787 Tegen, I., Schepanski, K.: The Global distribution of Mineral Dust, *IOP Conference Series: Earth and Environ-*
788 *mental Sciences*, 7, 012001, [doi:10.1088/1755-1307/7/1/012001](https://doi.org/10.1088/1755-1307/7/1/012001), 2009.
- 789 Tyson, P. D. and Preston-Whyte, R. A.: *The Weather and Climate of Southern Africa*, 2nd ed., Oxford University
790 Press Southern Africa, Cape Town, 2014.
- 791 Ventura, A., Simões, E.F.C., Almeida, A.S., Martins, R., Duarte, A.C., Loureiro, S., Duarte, R.M.B.O., Deposition
792 of aerosols onto upper ocean and their impacts on marine biota, *Atmosphere*, 12, 684,
793 <https://doi.org/10.3390/atmos12060684>, 2021.
- 794 Vickery, K.J., Eckardt, F.D.: Dust emission controls on the lower Kuseb River valley, Central Namib, *Aeolian*
795 *Res.*, 10, 125-133, <https://doi.org/10.1016/j.aeolia.2013.02.006>, 2013.
- 796 von Holdt, J.R., Eckardt, F.D., Wiggs, G.F.S.: Landsat identifies aeolian dust emission dynamics at the landform
797 scale, *Remote Sensing Environ.*, 198, 229-243, <https://doi.org/10.1016/j.rse.2017.06.010>, 2017.
- 798 Wozniak, A. S.; Shelley, R. U.; Sleighter, R. L.; Abdulla, H. A. N.; Morton, P. L.; Landing, W. M.; Hatcher, P. G.
799 Relationships among aerosol water soluble organic matter, iron and aluminium in European, North African,
800 and Marine air masses from the 2010 US GEOTRACES cruise, *Mar. Chem.*, 154, 24– 33 DOI: 10.1016/j.mar-
801 chem.2013.04.011, 2013.
- 802 Wozniak, A. S., R.U. Shelley, S.D. McElhenie, W.M. Landing, P. G. Hatcher. Aerosol water soluble organic
803 matter characteristics over the North Atlantic Ocean: Implications for iron-binding ligands and iron solubility.
804 SCOR WG 139: Organic Ligands – A Key Control on Trace Metal Biogeochemistry in the Ocean 173: 162-72.
805 <https://doi.org/10.1016/j.marchem.2014.11.002>, 2015.
- 806 Zhuang, G., Z. Yi, R. A. Duce, and Brown, P.R.: Link between iron and sulphur cycles suggested by detection
807 of Fe (II) in remote marine aerosols, *Nature*, 355, pp. 537–539, <https://doi.org/10.1038/355537a0>, 1992.
- 808
- 809